PIER M

(Received 23 December 2024, Accepted 10 February 2025, Scheduled 20 February 2025)

Research on the Simulation Method of the Security Check Scene Based on Passive Millimeter-Wave Imaging

Chuan Yin[1], Siyi Zhang[1,*], Pengpeng Xu[1], and Hong Kuan[2]

[1] *School of Microelectronics, Hangzhou Dianzi University, Hangzhou, China*
[2] *Beijing Furun Cheng Lighting System Engineering Co., Ltd., Beijing, China*

ABSTRACT: Current research on passive millimeter wave (PMMW) human security imaging mainly focuses on system optimization and image processing algorithms, with limited attention on simulation studies. This paper addresses this gap by developing a PMMW imaging simulation for human security screening. The study proposes a Multi-layer Brightness Temperature Tracing Method (MBTTM) to accurately calculate brightness temperature values across various scattering directions. The paper proposes a simulation model for microrough surfaces based on the rough characteristics of human skin in security check scenarios. It also presents a PMMW brightness simulation model for detecting hidden dangerous goods in hierarchical media. The model incorporates diffuse ray tracking and accounts for transmission phenomena when rays interact with penetrable surfaces. Finally, both simulation and experimental validation are conducted for human security scenes. Experimental results demonstrate the effectiveness of the proposed method in detecting concealed objects, with a detailed analysis of the impact of surface roughness, ray spacing, and concealment depth on imaging quality.

1. INTRODUCTION

In the 1990s, the U.S. Pacific Northwest National Laboratory pioneered the development of a millimeter-wave security screening system, utilizing millimeter-wave holographic imaging for human body security scanning [1, 2]. An imaging algorithm [3] using wide bandwidth was proposed to eliminate the speckle effect in single-frequency imaging. Later, computerized reconstruction algorithms [4, 5] built 3D images and incorporated polarization principles, distinguishing smooth and sharp features to identify hidden objects. In the same year, a cylindrical scanning system was introduced, enabling all-around, dead-angle-free scanning. R&S Germany then proposed a new passive millimeter-wave imaging system for real-time operational imaging [6, 7]. German scientists also noted the significant impact of reflective backgrounds on imaging results [8]. Recent advancements in millimeter-wave security screening systems include image segmentation, edge contour recognition using Dynamic Time Warping [9], body contour estimation algorithms for detecting hidden metals and water-based substances [10], and the Non-uniform Fast Fourier Transform for sharper edges and reduced noise [11]. Compression holographic imaging [12] reduces antenna units and data sampling time, while a multi-hazardous object recognition method [13] aids in hazardous object detection. A deep learning-based system for detecting hidden hazardous materials [14] was also developed.

Despite these advancements, there remain significant challenges in millimeter-wave imaging for security screening. One major limitation is the accurate modeling of human skin and other surfaces in security scenarios. Traditional approaches often oversimplify these surfaces, leading to discrepancies between simulated and actual imaging results.

Compared to the measured results of the millimeter-wave security imaging system, the simulated results of passive millimeter-wave radiation imaging exhibit higher resolution. This paper conducts passive millimeter-wave radiation imaging simulations for security screening scenarios. Human skin in security scenes, treated as micro-rough surfaces, is often inaccurately modeled as deep rough or smooth surfaces [15, 16], leading to errors in the simulated and actual brightness temperature distributions. Furthermore, existing methods for brightness temperature tracking often fail to account for the complex scattering behaviors of rough surfaces, particularly in security scenarios where hidden objects may be present. This limitation necessitates a more sophisticated approach to accurately model the interaction of millimeter waves with various surfaces and materials. To simulate imaging of rough scene models, it is essential to extend the traditional brightness temperature tracking method by incorporating diffuse ray tracking. This paper proposes an enhanced Multi-layer Brightness Temperature Tracing Method to more accurately calculate brightness temperature values across various scattering directions. Additionally, in security scenarios, it is necessary to account for transmission phenomena when rays interact with penetrable surfaces. Consequently, this paper improves the hierarchical medium brightness temperature imaging model, expanding it to simulate imaging of various hidden hazardous materials in security screening scenarios. These improvements aim to bridge the gap between theoretical simulations and practical imaging results, ultimately enhancing the effectiveness of millimeter-wave imaging in real-world security applications.

* Corresponding author: Siyi Zhang (222040170@hdu.edu.cn).

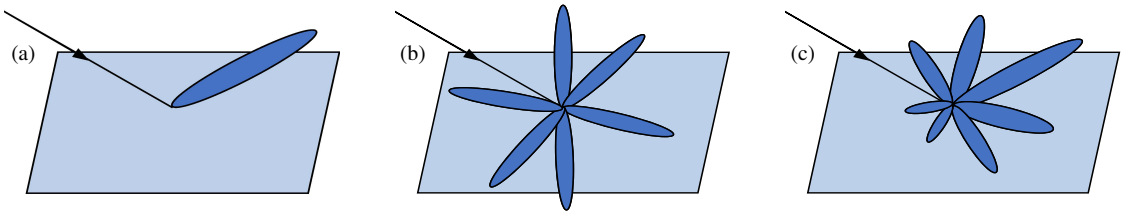

FIGURE 1. Ray reflection model. (a) Smooth plane model. (b) Lambert's approximation model. (c) Optimization model.

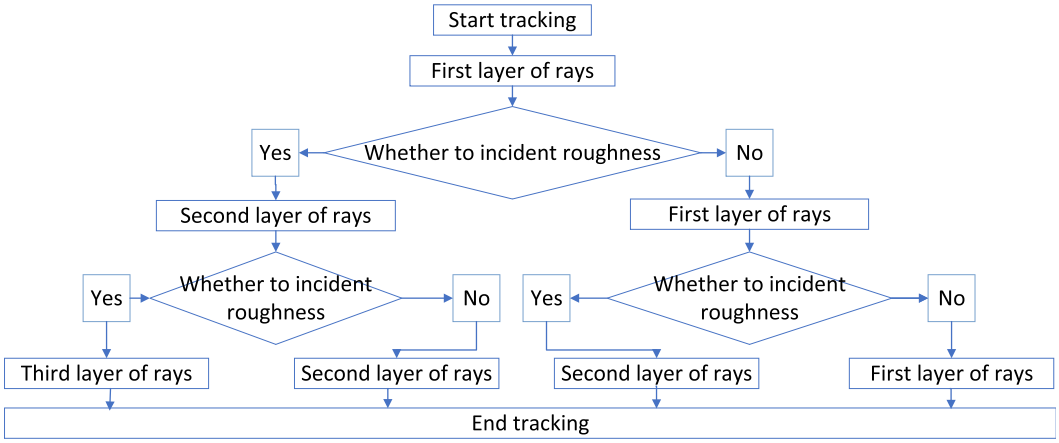

FIGURE 2. Radiation layering flowchart.

2. MULTI-LAYER BRIGHTNESS TEMPERATURE TRACKING METHOD

Taking into account the diffuse reflection that occurs when the ray strikes a rough surface, an optimization model is developed based on the smooth surface and Lambertian approximation models. In this model, the brightness temperature of scattering in all directions varies, with the highest temperature observed in the direction closest to specular reflection. As the scattering direction deviates from the specular reflection angle, the brightness temperature progressively decreases. The model is illustrated in Figure 1.

2.1. The Basic Idea of MBTTM

To trace diffuse rays, it is essential to stratify all rays emitted from the radiometer. Ray tracing is terminated when the ray reaches the maximum number of diffuse reflections. By setting a higher maximum reflection count, the accuracy of the simulated brightness temperature is improved, and the simulation values become closer to the actual measurements. The layered flowchart for ray tracing is shown in Figure 2.

3. HIERARCHICAL MEDIUM BRIGHT TEMPERATURE MODEL

3.1. Hierarchical Medium Bright Temperature Tracking Model

Figure 3 illustrates an air-to-body detection model for concealed objects. A radiometer detects the human body near the abdomen, with the target object concealed beneath the clothing, as shown in Figure 4. In the millimeter-wave band, human

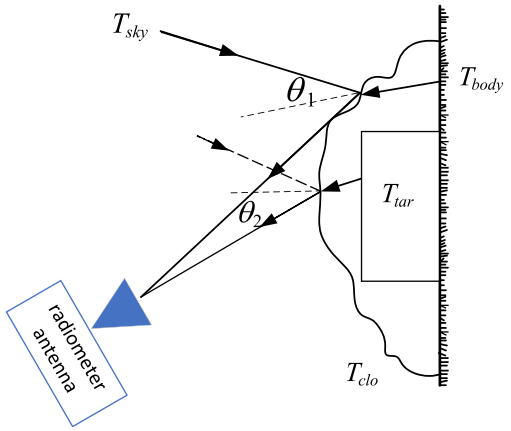

FIGURE 3. Airborne human detection of hazardous substances physical model.

clothing and skin are modeled as rough surfaces, while concealed objects such as knives and pistols are treated as smooth surfaces. Clothing, due to its high transmittance, is considered a transmissive layer. The model represents a typical hierarchical medium with three layers: air layer, clothing layer, and human skin layer. The physical temperatures of the human body, clothing, and concealment (T_{body}, T_{clo}, and T_{tar}) are assumed equal ($T_{body} = T_{clo} = T_{tar}$) to reflect realistic conditions. The radiometer receives brightness temperatures from two directions: θ_1, which includes contributions from the atmosphere, clothing, hidden object, and their interactions, and θ_2, which incorporates the human skin, clothing, and atmosphere. Atmospheric brightness reaches the radiometer via diffuse reflection from the

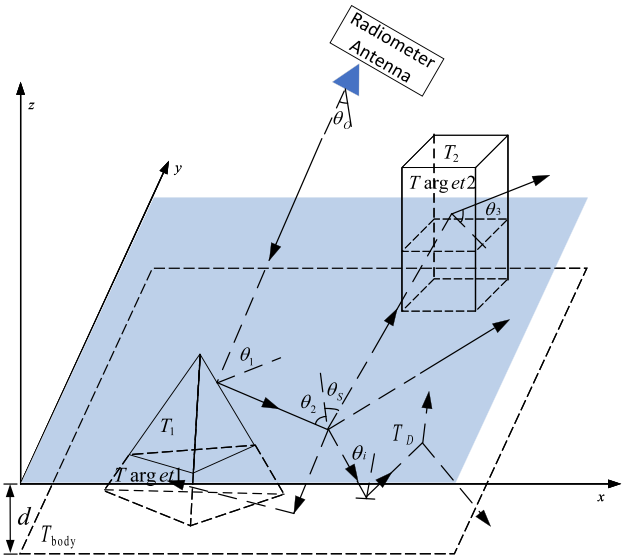

FIGURE 4. Airborne human hierarchical medium brightness temperature tracking model.

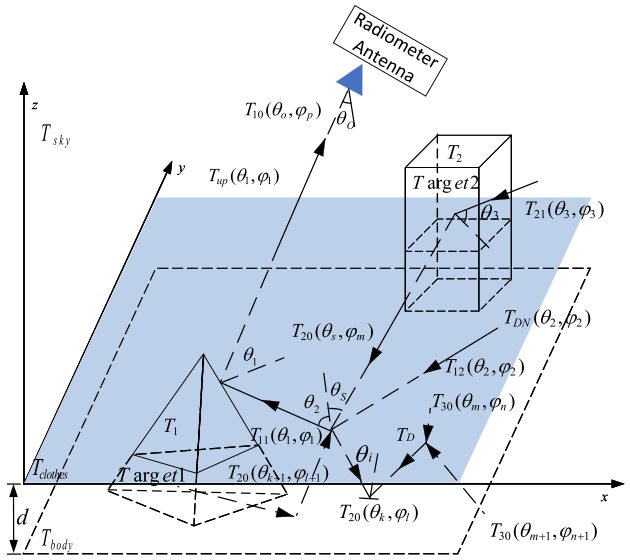

FIGURE 5. Airborne human hierarchical medium brightness temperature inversion model.

clothing, while the brightness from hidden objects, skin, and clothing arrives through diffuse transmission. Figure 4 depicts the hierarchical dielectric bright-temperature tracking model for a single ray. There are three media in Figure 4: (1) when $z > 0$, the medium is the atmosphere; (2) when $-d < z < 0$, the medium is clothing; and (3) when $z < -d$, the medium is human skin. Two cloaked objects were placed between human skin and clothing, which were treated as rough surfaces in the millimeter-wave band, with the human skin set as a Gaussian-type slightly rough surface and the clothing as a Gaussian-type deeply rough surface. If the concealed objects were metallic, they were considered as smooth surfaces. The rays are emitted from the radiometer port, and unlike the multilayer bright-temperature tracking model in the previous section, in the air-to-body bright-temperature tracking model in this section, two things happen when the rays are incident on the rough surface of the clothing: a diffuse reflection phenomenon occurs, where the rays propagate into the atmospheric background of $z > 0$, and a diffuse transmittance phenomenon occurs, where the rays propagate into the clothing layer of $-d < z < 0$.

In Figure 4, because the ray needs to experience the phenomenon of reflection or transmission, when the ray reflects or transmits, it intersects the surface of the new source point and launches the ray into the surrounding area. The new ray, upon encountering the rough surface and transmissive layer, will continue to repeat the above operation. At this stage, the ray analysis becomes more complicated, and ray stratification is used to manage the tracing process. The brightness temperature of the rays is denoted by T_{ij}, which indicates the number of layers of rays ($1 \leq i \leq 3$) and the number of reflections or transmissions of the rays ($0 \leq j \leq 3$).

3.2. Hierarchical Medium Brightness Temperature Inversion Model

Based on the bright temperature tracking method [15, 16], a corresponding hierarchical-type medium bright temperature inversion model is established. In this model, the end point of the tracking model serves as the source point, and the radiometer acts as the receiving point, as shown in Figure 5. The model must account for rays that experience diffuse reflection above the transmissive layer, as well as those that undergo diffuse transmission below it.

In Figure 5, $T_{10}(\theta_o, \varphi_p)$ represents the final received brightness temperature at the radiometer, which consists of the atmospheric background brightness temperature $T_{up}(\theta_1, \varphi_1)$, the brightness temperature $T_1 \cdot e_1(\theta_2)$ of concealed object 1 in the θ_1 direction, and the brightness temperature $T_{11}(\theta_1, \varphi_1) \cdot r_1(\theta_1)$ reflected by concealed object 1 in the θ_1 direction. Therefore, $T_{10}(\theta_o, \varphi_p)$ can be expressed as:

$$\begin{aligned} T_{10}(\theta_o, \varphi_p) &= T_1 \cdot e_1(\theta_1) + T_{11}(\theta_1, \varphi_1) \cdot r_1(\theta_1) \\ &\quad + T_{up}(\theta_1, \varphi_1) \end{aligned} \tag{1}$$

The first term in Equation (1) represents the brightness temperature of concealed object 1 in the θ_1 direction, where $e_1(\theta_1)$ denotes its emissivity in that direction. The second term in Equation (1) represents the brightness temperature from the human skin to concealed object 1, comprising three components: the brightness temperature from the skin, the brightness temperature from the rough clothing surface in the relevant direction, and the brightness temperature from the surrounding non-coherent directions. This is expressed by Equation (2):

$$\begin{aligned} T_{11}(\theta_1, \varphi_1) &= \Big[T_{12}(\theta_2, \varphi_2) \cdot r_{cp}(\theta_2) \cdot \mathrm{e}^{-4k^2\sigma^2\cos^2(\theta_2)} \\ &\quad + T_{sum}(\theta_2, \varphi_2) + T_c \cdot e_{cp}(\theta_2) \Big] \cdot D_{12}^1 \end{aligned} \tag{2}$$

Equation (2) consists of three parts: the first term represents the coherent component of the ray undergoing diffuse reflection; the second term corresponds to the incoherent component of the ray, which includes both diffuse reflection and transmission, i.e., the combination of brightness temperatures from the

surroundings; and the third term represents the brightness temperature of the clothing itself. Here, $r_{cp}(\theta_2)$ is the reflectivity of the clothing in the θ_2 direction, $e^{-4k^2\sigma^2\cos^2(\theta_2)}$ the roughness factor of the clothing, T_c the physical temperature of the clothing, and T_{sum} the sum of the brightness temperatures of the rays in the upper layer of the rough surface that reach concealed object 1 after diffuse reflection, i.e.:

$$T_{sum}(\theta_2,\varphi_2) = \sum_{i=1,M}\sum_{j=1,N} T_{20}(\theta_i,\varphi_j) \cdot\Gamma(\theta_i,\varphi_j;\theta_2,\varphi_2) \quad (3)$$

For the hierarchical medium rough surface model presented in this paper, T_{sum} must account not only for the brightness temperatures around the upper part of the incident layer, but also for the sum of the brightness temperatures of rays transmitted through the transmission layer below the incident layer to concealed object 1, i.e.,

$$T_{sum}(\theta_2,\varphi_2) = \sum_{i=1,M}\sum_{j=1,N} T_{20}(\theta_i,\varphi_j)\cdot\Gamma(\theta_i,\varphi_j;\theta_2,\varphi_2) + \sum_{k=1,M}\sum_{l=1,N} T_{20}(\theta_k,\varphi_l)\cdot\Gamma_t(\theta_k,\varphi_l;\theta_2,\varphi_2) \quad (4)$$

In the above equation, $T_{20}(\theta_i,\varphi_j)$ represents the brightness temperature of the human skin layer reaching the clothing layer, and $\Gamma_t(\theta_k,\varphi_l;\theta_2,\varphi_2)$ denotes the transmittance from direction (θ_k,φ_l) to (θ_2,φ_2), which is given by Equation (5):

$$\Gamma_{tp}(\theta_k,\varphi_l;\theta_2,\varphi_2) = \int_{\theta_2-\frac{\pi}{2M}}^{\theta_2+\frac{\pi}{2M}}\int_{\varphi_2-\frac{\pi}{2N}}^{\varphi_2+\frac{\pi}{2N}} \frac{[\sigma_{tpp}(\theta_k,\varphi_l;\theta,\varphi)+\sigma_{tpq}(\theta_k,\varphi_l;\theta,\varphi)]\cdot\sin(\theta)}{4\pi\cos(\theta_k)}\,d\varphi d\theta \quad (5)$$

$\Gamma(\theta_i,\varphi_j;\theta_2,\varphi_2)$ is the scattering rate from direction (θ_i,φ_j) to direction (θ_2,φ_2) and can be expressed as:

$$\Gamma_p(\theta_i,\varphi_j;\theta_2,\varphi_2) = \int_{\theta_2-\frac{\pi}{2M}}^{\theta_2+\frac{\pi}{2M}}\int_{\varphi_2-\frac{\pi}{2N}}^{\varphi_2+\frac{\pi}{2N}} \frac{[\sigma_{pp}(\theta_i,\varphi_j;\theta,\varphi)+\sigma_{pq}(\theta_i,\varphi_j;\theta,\varphi)]\cdot\sin(\theta)}{4\pi\cos(\theta_i)}\,d\varphi d\theta \quad (6)$$

In Equations (5) and (6), $\sigma_{tpp}(\theta_k,\varphi_l;\theta_2,\varphi_2)$ and $\sigma_{pp}(\theta_i,\varphi_j;\theta_2,\varphi_2)$ are the transmission and scattering coefficients of rays incident on the clothing, respectively, with p and q denoting the polarization modes.

In Equation (6), $T_{20}(\theta_k,\varphi_l)$ represents the lower ray of the clothing layer and can be expressed as:

$$T_{20}(\theta_k,\varphi_l) = (T_B\cdot e_b(\theta_k) + T_{21}(\theta_k,\varphi_l))\cdot e^{-\gamma d} \quad (7)$$

In the above formula, T_B is the brightness temperature of the human skin layer, $e_b(\theta_k)$ the emissivity of the human skin in the θ_k direction, γ the attenuation coefficient of the clothing layer, d the thickness of the clothing layer, and $T_{21}(\theta_k,\varphi_l)$ the brightness temperature emitted downward from the clothing layer and reflected in the direction of (θ_k,φ_l) by the human skin layer.

The emissivity of transmissive rough surfaces in the hierarchical media roughness model is calculated differently from that in the single-layer media model and can be expressed as:

$$e_{rp}(\theta_1) = 1 - {r_{rp}}^{coh}(\theta_1) - r_{rp}^{non}(\theta_1) \quad (8)$$

In contrast, for the hierarchical media model, the transmittance of the clothing layer must be considered, so the emissivity of the clothing layer is:

$$e_{rp}(\theta_1) = 1 - {r_{rp}}^{coh}(\theta_1) - r_{rp}^{non}(\theta_1) - t_{rp}(\theta_1) \quad (9)$$

where $t_{rp}(\theta_1)$ is denoted as the transmittance of the clothing layer in the θ_1 direction, which can be expressed by Equation (15):

$$t_{rp}(\theta_1) = \iint_{\Omega} \frac{[\sigma_{tpp}(\theta_1;\theta_k,\varphi_l)+\sigma_{tpq}(\theta_1;\theta_k,\varphi_l)]\cdot\sin(\theta_i)}{4\pi\cos(\theta_1)} d\theta_k d\varphi_l \quad (10)$$

Finally, the brightness temperature of radiation from the clothing layer to the concealed object 1, $T_{11}(\theta_2,\varphi_2)$, can be determined by combining Equations (2) and (10). As shown in the derivation of the brightness temperature $T_{10}(\theta_o,\varphi_p)$, the key to calculating the brightness temperature lies in determining the transmission coefficient of the transmissive layer. The following section outlines the method for calculating this transmission coefficient.

3.3. Derivation of Transmittance Coefficients for Deep Rough Surfaces

In this section, the transmission scattering problem of Gaussian-type deeply rough surfaces is addressed using Green's second theorem [17, 18] and the Kirchhoff standing phase method [19, 20].

As shown in Figure 6, a ray incident on the rough surface at the interface between medium I and medium II in direction θ_i undergoes transmission, with the transmitted ray propagating through medium II in direction θ_s. $\vec{k}_i$ is the unit vector of the incident ray direction, and $\vec{k}_s$ is the unit vector of the transmitted ray direction.

The two-base transmission scattering coefficient from medium I to medium II is derived using the Kirchhoff standing phase method and is expressed in Equation (11):

$$\sigma_{pq}^t = \frac{(\eta_1/\eta_2)\,(k_2\bar{q}\,|D_{pq}|)^2}{2\bar{q}^2\sigma^2\,|\rho''(0)|}\exp\left[-\frac{\bar{q}_x^2+\bar{q}_y^2}{2\bar{q}_z^2\sigma^2\,|\rho''(0)|}\right] \quad (11)$$

The transmission coefficient σ_o can be expressed by Equation (12):

$$\sigma_o = 10\log_{10}\sigma_{pq}^t \quad (12)$$

In Equations (11) and (12), η_1 and η_2 are the impedances of medium I and medium II, respectively. σ is the rms height of the incident roughness, k_2 the wave number of medium II, and

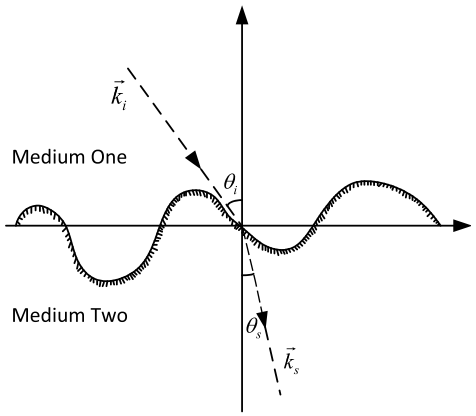

FIGURE 6. Schematic diagram of transmission scattering from a monolayer medium.

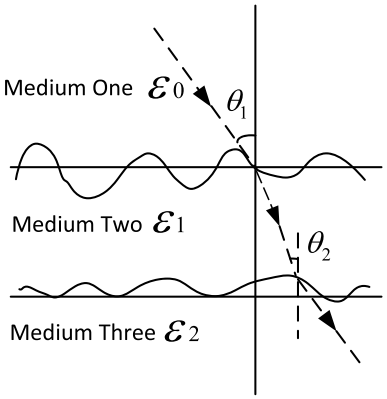

FIGURE 7. Hierarchical medium rough surface transmission model.

$\rho''(0)$ the second-order derivative of the roughness correlation function with respect to height undulation at 0. Gaussian-type roughness is defined as:

$$\rho''(0) = -\frac{2}{l^2} \tag{13}$$

In Equation (11), $\bar{q}_x$, $\bar{q}_y$, $\bar{q}_z$, and $\bar{q}$ can be expressed as respectively:

$$\begin{cases} \bar{q}_x = k_2 \sin\theta_s \cos\varphi_s - k_1 \sin\theta_i \cos\varphi_i \\ \bar{q}_y = k_2 \sin\theta_s \sin\varphi_s - k_1 \sin\theta_i \sin\varphi_i \\ \bar{q}_z = -k_2 \cos\varphi_s + k_1 \cos\varphi_i \\ \bar{q} = \sqrt{\bar{q}_x^2 + \bar{q}_y^2 + \bar{q}_z^2} \end{cases} \tag{14}$$

In Equation (14), θ_s and φ_s are the pitch and azimuth angles of the transmitted ray, respectively. θ_i and φ_i are the pitch and azimuth angles of the incident ray, respectively. D_{pq} in Equation (14) is the polarisation mode correlation coefficient, which can be expressed by Equation (15):

$$\begin{cases} D_{hh} = -\dfrac{2[k_2 - k_1(\vec{n}_i\cdot\vec{n}_s)]\left[T_\perp(\vec{v}_i\cdot\vec{n}_s)(\vec{v}_s\cdot\vec{n}_i) + T_{//}(\vec{h}_i\cdot\vec{n}_s)(\vec{h}_s\cdot\vec{n}_i)\frac{\eta_2}{\eta_1}\right]}{\bar{q}D_2\bar{D}_2} \\ D_{vh} = -\dfrac{2[k_2 - k_1(\vec{n}_i\cdot\vec{n}_s)]\left[T_\perp(\vec{v}_i\cdot\vec{n}_s)(\vec{h}_s\cdot\vec{n}_i) - T_{//}(\vec{h}_i\cdot\vec{n}_s)(\vec{v}_s\cdot\vec{n}_i)\frac{\eta_2}{\eta_1}\right]}{\bar{q}D_2\bar{D}_2} \\ D_{hv} = -\dfrac{2[k_2 - k_1(\vec{n}_i\cdot\vec{n}_s)]\left[T_\perp(\vec{h}_s\cdot\vec{n}_i)(\vec{h}_i\cdot\vec{n}_s) + T_{//}(\vec{v}_s\cdot\vec{n}_i)(\vec{v}_i\cdot\vec{n}_s)\frac{\eta_2}{\eta_1}\right]}{\bar{q}D_2\bar{D}_2} \\ D_{vv} = -\dfrac{2[k_2 - k_1(\vec{n}_i\cdot\vec{n}_s)]\left[T_\perp(\vec{v}_s\cdot\vec{n}_i)(\vec{h}_i\cdot\vec{n}_s) - T_{//}(\vec{h}_s\cdot\vec{n}_i)(\vec{v}_i\cdot\vec{n}_s)\frac{\eta_2}{\eta_1}\right]}{\bar{q}D_2\bar{D}_2} \end{cases} \tag{15}$$

In the above equations,

$$\begin{cases} T_{//} \approx T_{//0} + T_{//1}(Z_x\cos\varphi_i + Z_y\sin\varphi_i) \\ \quad = 1 + R_{//0} + R_{//1}(Z_x\cos\varphi_i + Z_y\sin\varphi_i) \\ T_\perp \approx T_{\perp0} + T_{\perp1}(Z_x\cos\varphi_i + Z_y\sin\varphi_i) \\ \quad = 1 + R_{\perp0} + R_{\perp1}(Z_x\cos\varphi_i + Z_y\sin\varphi_i) \end{cases} \tag{16}$$

$$\begin{cases} \vec{n}_i\cdot\vec{n}_s = \sin\theta_i\cos\varphi_i\sin\theta_s\cos\varphi_s \\ \qquad + \sin\theta_i\sin\varphi_i\sin\theta_s\cos\varphi_s + \cos\theta_i\cos\theta_s \\ \vec{v}_s\cdot\vec{n}_i = -\sin\theta_i\cos\theta_s\cos(\varphi_s - \varphi_i) + \cos\theta_i\sin\theta_s \\ \vec{v}_i\cdot\vec{n}_s = -\cos\theta_i\sin\theta_s\cos(\varphi_s - \varphi_i) + \sin\theta_i\cos\theta_s \\ \vec{h}_s\cdot\vec{n}_i = \vec{n}_i\cdot\vec{h}_s = -\sin\theta_t\sin(\varphi_s - \varphi_i) \\ \vec{h}_i\cdot\vec{n}_s = \sin\theta_s\sin(\varphi_s - \varphi_i) \end{cases} \tag{17}$$

$$\begin{cases} D_2 = \left|(\vec{n}_i\cdot\vec{n}_s)^2 + (\vec{n}_i\cdot\vec{h}_s)^2\right| \\ \bar{D}_2 = \bar{q}_z D_2 / |\bar{q}_z| \end{cases} \tag{18}$$

In Equation (16), Z_x and Z_y denote the root-mean-square slopes in the axial and transverse directions, respectively. $T_{//0}$ and $T_{\perp0}$ represent the 0th-order transmission coefficients of the transmissive layer for horizontal and vertical polarization, respectively. $T_{//1}$ and $T_{\perp1}$ denote the 1st-order transmission coefficients for horizontal and vertical polarization. Similarly, $R_{//0}$, $R_{\perp0}$, $R_{//1}$, and $R_{\perp1}$ are the 0th- and 1st-order reflection coefficients for horizontal and vertical polarizations, respectively.

In Figure 7, a ray is incident on the rough surface between medium I and medium II at direction θ_1, and the transmitted wave propagates from medium II into medium III at direction θ_2. The reflection coefficient of the model can be expressed as:

$$\begin{cases} R_{//0} = \frac{R_{oh} + R'_h}{1 + R_{oh}\cdot R'_h} \\ R_{\perp0} = \frac{R_{ov} + R'_v}{1 + R_{ov}\cdot R'_v} \end{cases} \tag{19}$$

In Equation (19), R_{oh} and R_{ov} denote the horizontally and vertically polarized reflection coefficients from medium I to medium II, respectively, and are given by:

$$\begin{cases} R'_{oh} = \frac{\cos\theta_1 - \sqrt{\varepsilon - \sin^2\theta_1}}{\cos\theta_1 + \sqrt{\varepsilon - \sin^2\theta_1}} \\ R'_{ov} = \frac{\varepsilon\cos\theta_1 - \sqrt{\varepsilon - \sin^2\theta_1}}{\varepsilon\cos\theta_1 + \sqrt{\varepsilon - \sin^2\theta_1}} \end{cases} \tag{20}$$

In Equation (19), R'_h and R'_v denote the horizontally and vertically polarized reflection coefficients from the intermediate

FIGURE 8. 3 mm passive millimetre wave imaging system.

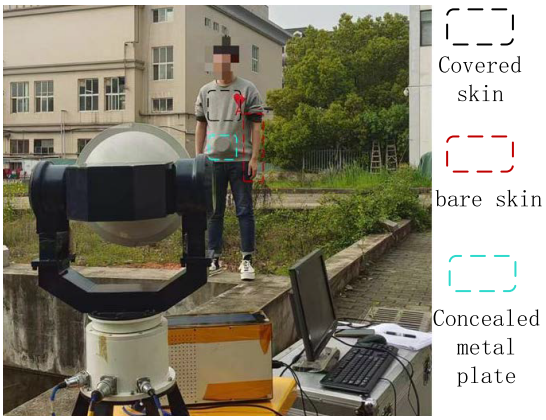

FIGURE 9. Optical images of outdoor scenes for human security screening.

TABLE 1. Experimental scene and millimeter-wave imaging system parameter configuration.

Parameter	Configuration	Parameter	Configuration
Azimuth pixel	120	Radiometer scanning interval	0.25°
Elevation pixel	90	Radiometer vertical distance	167 cm
Elevation center	0°	Radiometer horizontal distance	200 cm
Azimuth center	0°	Radiometer center frequency	94 GHz
Human height	175 cm	Cold source calibration brightness temperature	78 K
Human temperature	310 K	Hot source calibration brightness temperature	300 K
Metal piece size	12 cm × 12 cm	Metal piece temperature	300 K

dielectric layer to the lowermost dielectric layer, respectively, and are expressed as:

$$\begin{cases} R'_h(\theta_2) = R_{1h}(\theta_2)\exp(2ikH\sqrt{\varepsilon_1 - \sin^2\theta_2}) \\ R'_v(\theta_2) = R_{1v}(\theta_2)\exp(2ikH\sqrt{\varepsilon_1 - \sin^2\theta_2}) \end{cases} \tag{21}$$

In the above equation, R_{1h} and R_{1v} denote the horizontally polarised and vertically polarised reflection coefficients from the second layer of medium to the third layer of medium respectively, which can be expressed as:

$$\begin{cases} R_{1h}(\theta_2) = \dfrac{\sqrt{\varepsilon_1-\sin^2\theta_2}-\sqrt{\varepsilon_2-\sin^2\theta_2}}{\sqrt{\varepsilon_1-\sin^2\theta_2}+\sqrt{\varepsilon_2-\sin^2\theta_2}} \\ R_{1v}(\theta_2) = \dfrac{\varepsilon_2\sqrt{\varepsilon_1-\sin^2\theta_2}-\varepsilon_2\sqrt{\varepsilon_2-\sin^2\theta_2}}{\varepsilon_2\sqrt{\varepsilon_1-\sin^2\theta_2}+\varepsilon_2\sqrt{\varepsilon_2-\sin^2\theta_2}} \end{cases} \tag{22}$$

The association of Equations (19) to (22) can be used to find $R_{//0}$ and $R_{\perp 0}$. The first order reflection coefficient can be expressed as Equations (23):

$$\begin{cases} R_{//1} = -\dfrac{(\eta_1\sin\theta_1-\eta_2\sin\theta_2)-R_{//0}(\eta_1\sin\theta_1+\eta_2\sin\theta_2)}{\eta_1\cos\theta_1+\eta_2\cos\theta_2} \\ R_{\perp 1} = -R_{\perp 0}\dfrac{\eta_2\sin\theta_1+\eta_1\sin\theta_2}{\eta_2\cos\theta_1+\eta_1\cos\theta_2} \end{cases} \tag{23}$$

Assuming that Gaussian-type deep rough surfaces are isotropic rough surfaces, there are:

$$\left\{ Z_x = Z_y = \sqrt{\sigma^2\left|\rho''(0)\right|} \right. \tag{24}$$

The transmission and reflection coefficients of the rough surface of a layered medium can be found by combining the above equations.

4. EXPERIMENTS AND ANALYSIS

4.1. Human Security Scene Imaging Experiment

To validate the passive millimetre-wave radiation bright temperature simulation model for human security screening presented in this study, imaging experiments were conducted using the 3 mm millimetre-wave imaging system shown in Figure 8. The experimental setup, depicted in Figure 9, involved placing a metal object on the abdomen as a concealed hazardous material, with the top of the object covered by fabric. To examine the variations in radiant bright temperature as the human skin is affected by the fabric, the human arm was left exposed.

The outdoor temperature on the day of the experiment was approximately 20°C. The remaining parameters of the imaging system and experimental setup are provided in Table 1.

The experimental results, shown in Figure 10, reveal that the low resolution and sensitivity of the millimetre-wave imaging system reduce the contrast between the human body's bright temperature and that of the surrounding environment, resulting in a blurred human body silhouette. The figure also illustrates the low bright temperature of the concealed metal object, primarily influenced by surrounding environmental and human

TABLE 2. Imaging simulation parameter configuration.

Parameter	Configuration	Parameter	Configuration
Azimuth center	0°	Radiometer horizontal distance	200 cm
Elevation center	0°	Radiometer vertical distance	167 cm
Azimuth pixel	400	Radiometer scanning interval	0.05°
Elevation pixel	400	Radiometer center frequency	94 GHz
Human height	175 cm	System noise	1 K
Human temperature	310 K	Relative complex permittivity of the human body	$7.1 - j3.6$
Metal hexahedron temperature	300 K	Relative complex permittivity of the fabric	$3.98 - j0.01$

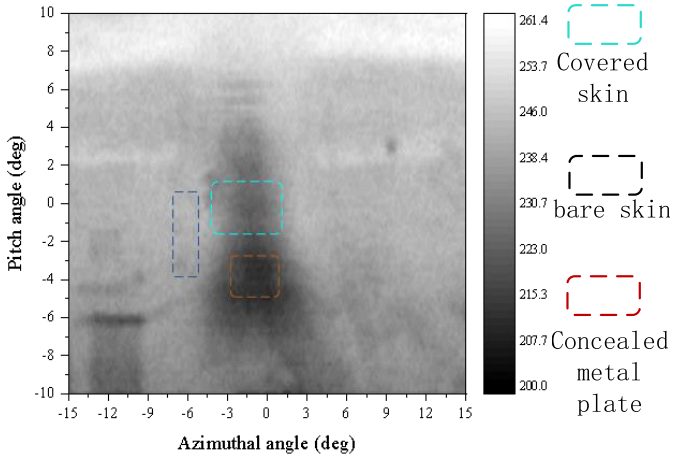

FIGURE 10. 3 mm human security scene measurement.

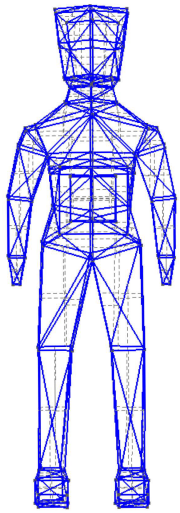

FIGURE 11. Human security virtual scene models.

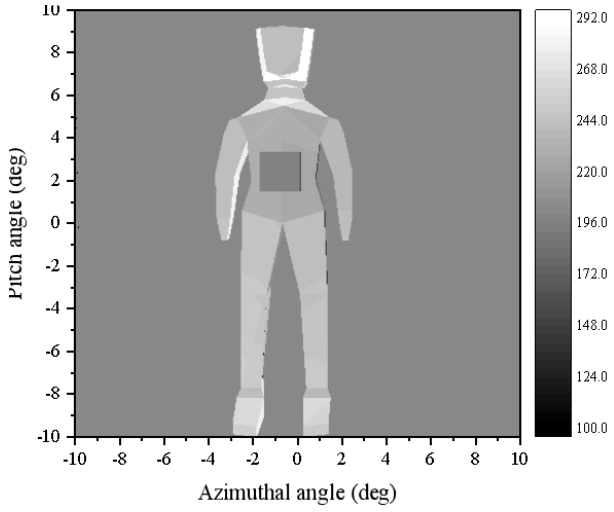

FIGURE 12. Human security scene simulation mock-up.

radiation, due to the metal's high reflectivity. The radiometer antenna's limitations cause the bright temperature in the arm region to closely resemble the outdoor environment, making it difficult to distinguish. However, by comparing with the optical image of the scene, the arm's position and bright temperature can still be confirmed. Overall, the bright temperature in the arm region is higher than that of the torso, confirming that the bright temperature of body radiation penetrating the fabric is attenuated.

After conducting the outdoor human security scene imaging experiments, a simulation of the experimental setup in Figure 9 was performed to verify the effectiveness of the human security scene model and its imaging method. A virtual model of the human security screening scene, as shown in Figure 11, was created, consisting of 160 points and 473 surface elements. A rough transmissive surface layer, simulating human clothing, was added to the abdomen of the human model, with roughness parameters set to ($\sigma = 3.5\lambda, l = 12\lambda$) and the human body surface roughness set to ($\sigma = 0.12/k, l = 2.8/k$). A hexahedron, placed 0.5 cm behind the transmissive surface, was used to simulate a hidden metal sheet with a reflectivity of 0.99. To enhance the contrast between the mannequin and atmospheric background, the background temperature was set to 200 K. The parameters for the imaging simulation are provided in Table 2.

A simulation of the human security screening scenario is shown in Figure 12. The simulation results demonstrate that the human security screening model and its imaging method effectively replicate the experimental scene. The brightness temperature of bare human skin is higher than that of the skin covered by fabric, while the brightness temperature of hidden metal objects is lower than that of the human body due to the metal's high reflectivity.

To further assess the accuracy of the simulation, a comparison was made between the measured and simulated brightness temperature values for bare skin, covered skin, and hidden metal. The average brightness temperatures for these areas were compared, as shown in Figure 13.

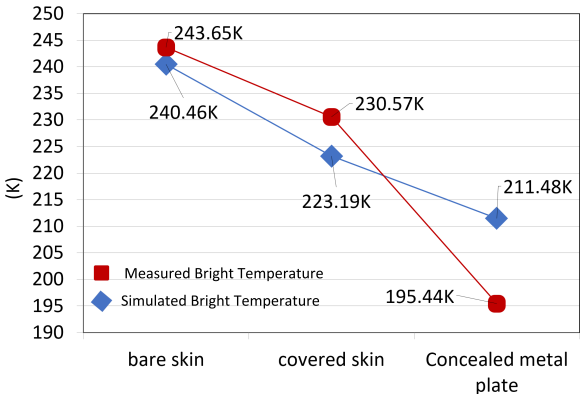

FIGURE 13. Comparison of measured and simulated bright temperatures.

Figure 13 shows a discrepancy between the bright temperature predicted by the human security model and the measured bright temperature. For bare skin, the simulation uses a microrough surface scattering model, which primarily accounts for reflection and diffuse reflection. This simplifies ray tracing and inversion, resulting in a small error of only 3 K between the measured and simulated bright temperatures. In contrast, for masked skin and hidden metal areas, the simulation applies a deep rough surface scattering transmission model, which accounts for more complex ray propagation in the actual scene. Consequently, the error increases, with relative errors of 7 K and 16 K, respectively. The discrepancies may be attributed to the following factors: The experimental scenario was conducted outdoors at a temperature of 20°C, where environmental factors such as wind could influence the experimental results, while the simulated scenario was set under idealized conditions with a background temperature of 200 K. In the experimental setup, the human model was exposed to different types of clothing, including bare skin and skin covered by fabric, whereas the simulated scenario utilized an idealized human model and clothing properties with specific roughness parameters applied. The experimental imaging system possesses sufficient sensitivity to distinguish temperature contrasts between skin, clothing, and the surrounding environment, and the simulated scenario also exhibits similar resolution, although it may not fully capture the noise and inconsistencies present in real-world conditions. The real-world experimental setup is affected by noise and inconsistencies, which can impact the accuracy of the results, whereas the simulation can accurately replicate results under ideal conditions, but discrepancies may still arise due to external factors.

4.2. Human Security Scene Simulation

To further analyze the variation in bright temperature of the concealment under different conditions, simulations were conducted using the human security screening scenario model in Figure 11. Pistols, ceramic knives, and petrol were placed behind the model fabric as concealed objects. The radiometer antenna was set to a 20° pitch and azimuth swing, operating at a frequency of 100 GHz. The relative complex permittivities used in the simulation were: human body, $7.1 - j3.6$ [21]; fabric, $3.98 - j0.01$ [22]; ceramic knife, $5.673 - j0.0085$ [23]; and petrol, $2.12 - j0.13$ [24]. The pistol was assigned a reflectivity of 0.99 due to its metal composition. The human body was modeled as a Gaussian-type slightly rough surface, while the fabric was modeled as a Gaussian-type deeply rough surface. The knife, petrol, and pistol were treated as smooth objects. The atmospheric temperature was set to 200 K, and the physical temperatures of the human body, concealed objects, and fabric were all set to 310 K.

4.2.1. The Effect of Ray Spacing on Bright-Temperature Analogue Imaging

To investigate the impact of ray number (i.e., ray spacing) on simulated bright temperature imaging, four simulations were conducted with varying ray intervals. As shown in Figures 14(a)–(d), the spatial resolutions (ray spacings) of the four simulations were $0.05°$, $0.1°$, $0.15°$, and $0.2°$, respectively. The concealed object in the simulation was a pistol, with the human body roughness parameters set to $(\sigma = 0.1/k, l = 3.0/k)$ and the fabric roughness parameters set to $(\sigma = 2.4\lambda, l = 10\lambda)$.

All four simulations in Figure 14 effectively reproduce the virtual scene, with the mannequin clearly outlined and a distinct difference in bright temperature between the pistol concealed behind the fabric and the exposed surface of the body. The area of the human body covered by fabric shows a lower brightness temperature than the uncovered regions, indicating that the clothing attenuates the emitted and reflected radiation from the body, thus validating the transmission model. As the ray interval increases, image clarity decreases, with the boundaries of the human body, background, and pistol becoming less distinct, eventually leading to distortion that hampers accurate target shape recognition.

From the simulation results in Figure 14, it can be observed that as the ray spacing decreases from $0.2°$ to $0.1°$, the image clarity and edge details are significantly improved, especially at larger spacings (such as $0.2°$), where the target contours are relatively blurred. However, when the spacing is further reduced to $0.05°$, although image details improve, the rate of improvement gradually decreases, particularly in the boundary regions, where the changes become more subdued. This indicates that after a certain point, further decreasing the ray spacing leads to diminishing returns in terms of image quality improvement.

Therefore, in practical applications, it is not advisable to blindly pursue the smallest possible ray spacing. Instead, a reasonable spacing should be chosen based on the specific application scenario and computational resource constraints. For example, in this simulation, a ray spacing of $0.1°$ is sufficient to ensure image quality while avoiding unnecessary computational costs, thereby balancing computational efficiency with image accuracy.

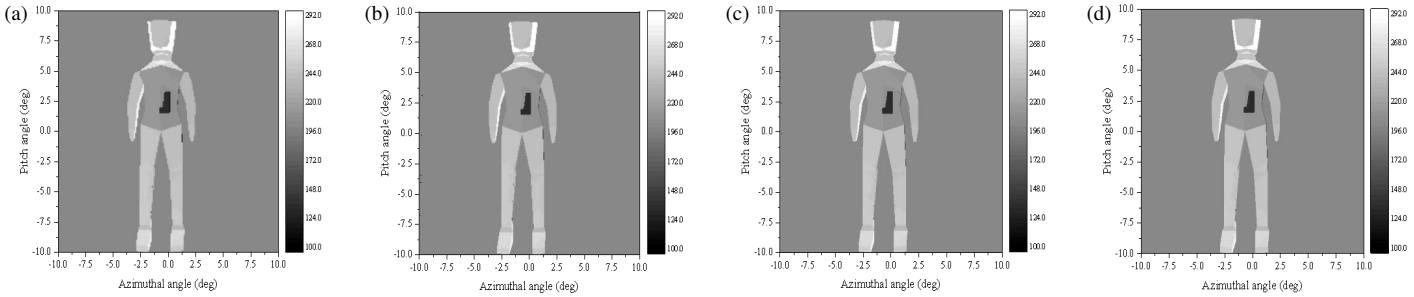

FIGURE 14. Simulated imaging of bright temperatures obtained at different ray intervals. (a) Radiation spacing of $0.2°$. (b) Radiation spacing of $0.15°$. (c) Radiation spacing of $0.1°$. (d) Radiation spacing of $0.05°$.

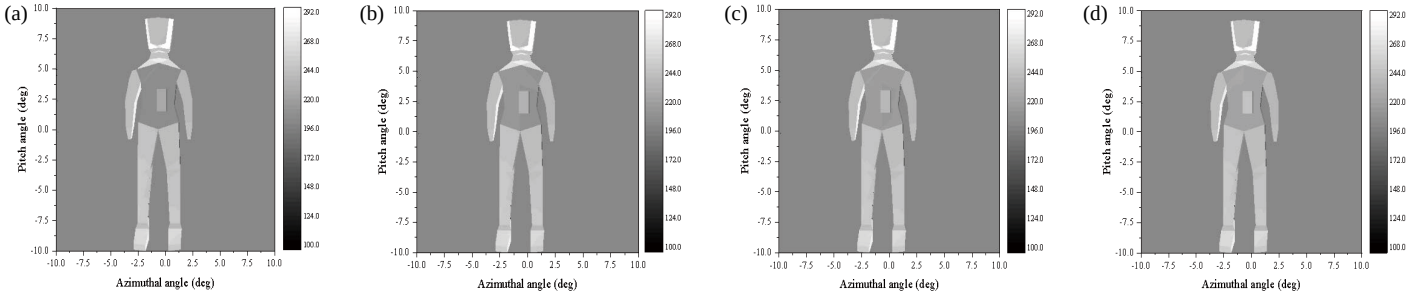

FIGURE 15. Simulation of human security bright temperature at different rms heights. (a) $\sigma = 1.8\lambda$. (b) $\sigma = 2.4\lambda$. (c) $\sigma = 3.0\lambda$. (d) $\sigma = 3.6\lambda$.

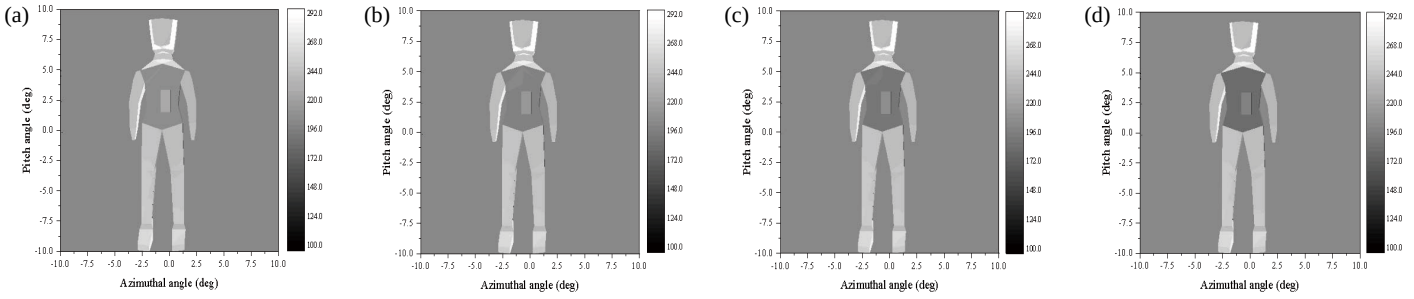

FIGURE 16. Simulation of human security screening with different correlation lengths. (a) $l = 10\lambda$. (b) $l = 12\lambda$. (c) $l = 14\lambda$. (d) $l = 18\lambda$.

4.2.2. Simulation of Bright Temperature Imaging of Cryptids at Different Levels of Roughness

To investigate the impact of deep roughness transmission surfaces on the bright-temperature imaging simulations for human security screening at varying root-mean-square heights, the root-mean-square height σ of the fabric was set to 1.8λ, 2.4λ, 3.0λ, and 3.6λ, with the corresponding length fixed at 10λ and the concealed hazard set to petrol. The resulting bright-temperature simulation is shown in Figures 15(a)–(d).

In Figure 15, all four images of the virtual scene show a distinct boundary between the human body contour and the petrol to be measured. As the root-mean-square height of the fabric increases, with the fabric length held constant, the bright temperature of both the human body and petrol regions gradually increases. This effect is primarily due to the increased roughness of the fabric, which enhances the transmission coefficient and reduces the attenuation of bright temperatures from the fabric's backside, leading to higher temperatures detected by the radiometer.

To examine the impact of deep roughness transmission surfaces on the bright-temperature imaging simulation for human security screening under varying correlation lengths, the root-mean-square height σ of the fabric was fixed at 1.8λ, with the correlation lengths set to 10λ, 12λ, 14λ, and 16λ. The concealed hazard is set to petrol, and the simulation results are shown in Figures 16(a)–(d).

In Figure 16, as the correlation length increases (i.e., the fabric becomes smoother) while keeping the root-mean-square height constant, the transmission coefficient of the fabric decreases, resulting in lower bright temperatures for both the fabric-covered human body and the petrol.

In summary, for the human security screening model, when the relative permittivity of the covering surface and the physical temperatures of the atmospheric background, human body, and concealed hazards are constant, rougher surfaces result in higher transmitted brightness temperatures, making the simulation appear brighter. Conversely, smoother surfaces reduce transmitted brightness temperatures, causing the simulation to appear darker.

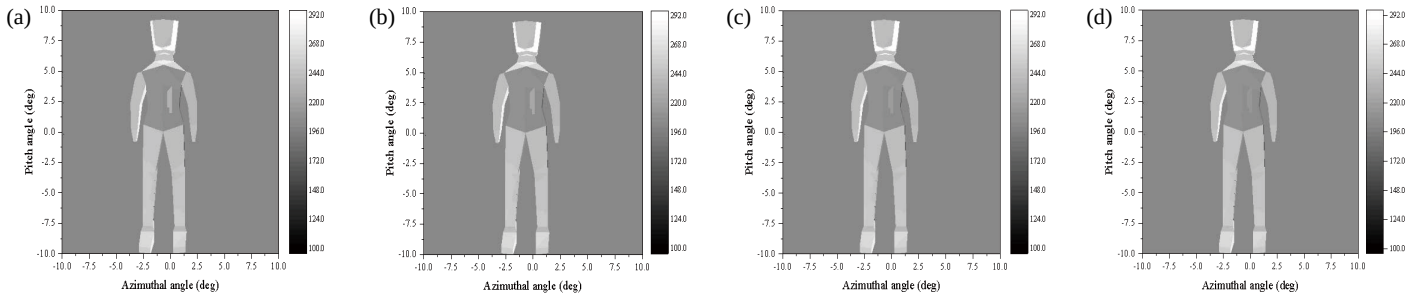

FIGURE 17. Simulation of bright temperature for human security screening at different depths of concealment. (a) $d = 0.5$ cm. (b) $d = 1$ cm. (c) $d = 2$ cm. (d) $d = 3$ cm.

4.2.3. Simulation of Bright Temperature Imaging of Cryptids at Different Depths of Concealment

In security applications, the fabric thickness and the hidden hazards behind the human body play a critical role in the propagation of thermal radiation. Both the attenuation caused by fabric transmittance and the damping of thermal radiation within the fabric layer must be considered. To investigate the impact of concealment depth on thermal imaging in human security screening, different concealment depths were modeled: $d = 0.5$ cm, $d = 1$ cm, $d = 2$ cm, and $d = 3$ cm. The concealed object, a knife, was used in the simulation, with results shown in Figures 17(a)–(d).

In Figure 17, at a concealment depth of $d = 0.5$ cm, the attenuation of the tool's thermal radiation is minimal, maintaining a clear distinction between the body and the tool. However, as the concealment depth increases, the propagation path of the tool's thermal radiation through the fabric layer lengthens, leading to greater attenuation. Consequently, the thermal radiation reaching the radiometer is reduced. At $d = 3$ cm, the thermal emissions from the tool and the body become indistinguishable, obscuring the boundary between the two.

5. CONCLUSION

This paper presents a passive millimeter-wave imaging simulation and experimental study for human security screening, focusing on bright temperature calculation and image simulation within the context of passive millimeter-wave remote sensing and detection.

A multi-layer bright temperature tracking model and its inverse model are developed to simulate the thermal radiation of rough surfaces, based on the roughness of human skin in security contexts. Simulation results indicate that bright temperature increases with surface roughness. Additionally, for constant roughness, the bright temperature varies with changes in the medium, surface type, and polarization mode.

A passive millimeter-wave bright temperature calculation model for concealed dangerous goods is developed based on security inspection scenarios. A hierarchical medium bright temperature tracking model and its inverse are established, with the Kirchhoff standing phase method used to compute the transmission coefficient for Gaussian deep roughness. Bright-temperature imaging simulations of typical concealed hazards — knives, handguns, and gasoline — are performed, examining the effects of fabric roughness, ray spacing, and concealment depth on imaging. Simulation results demonstrate distinct bright temperatures for the human body, knives, handguns, and gasoline, confirming the model's effectiveness in security screening. Increasing fabric roughness enhances the transmitted bright temperature, while deeper concealment reduces the transmitted bright temperature, aligning it closer to the human body's thermal radiation.

Imaging experiments for human security screening were conducted, and the measured results were compared with the simulated outcomes. This comparison verifies the effectiveness of the security screening model and imaging method, while also analyzing the error between the simulated and measured values.

The results of this study are of significant importance for improving the efficiency and accuracy of security screening in public safety systems. As a non-contact, non-radiative detection method, passive millimeter-wave imaging technology can effectively distinguish between the human body and concealed hazardous items, such as knives, firearms, and liquids. Particularly in high-traffic areas such as airports and train stations, this technology can significantly enhance the speed of security checks, reduce human error, and mitigate security risks. Through the brightness temperature (brightness temperature) calculation model, we can accurately simulate the thermal radiation characteristics of the human body and objects, providing reliable technical support for security personnel. Furthermore, the impact of factors such as fabric roughness, line spacing, and concealment depth on the brightness temperature offers valuable insights for optimizing parameters in practical security screening. In the future, this technology can be further extended to applications in large-scale event security and border control, thereby improving overall safety management.

Although the model proposed in this study has shown good performance in simulations and experiments, there are still certain limitations. First, the model assumes simplified roughness and surface types, whereas in reality, the brightness temperature differences between materials may be more complex. Second, the simulations in this study are based on idealized environments, and factors such as environmental noise and variations in lighting in actual security screening scenarios may affect the accuracy of the results. Future research should consider more complex environmental backgrounds and the impact of multi-band and multi-polarization modes to further improve the robustness and adaptability of the model. Additionally, integrat-

ing artificial intelligence technologies could facilitate the development of real-time security screening systems, enhancing both the efficiency and intelligence of security checks.

REFERENCES

[1] McMakin, D. L., D. M. Sheen, H. D. Collins, T. E. Hall, and R. H. Severtsen, "Wideband millimeter-wave holographic weapons surveillance systems," in *Law Enforcement Technologies: Identification Technologies and Traffic Safety*, Vol. 2511, 131–141, 1995.

[2] Sheen, D. M., H. D. Collins, T. E. Hall, D. L. McMakin, R. P. Gribble, R. H. Severtsen, J. M. Prince, and L. D. Reid, "Real-time wideband holographic surveillance system," U.S. Patent 5,557,283, 1-25, 1996.

[3] Sheen, D. M., D. L. McMakin, and T. E. Hall, "Three-dimensional millimeter-wave imaging for concealed weapon detection," *IEEE Transactions on Microwave Theory and Techniques*, Vol. 49, No. 9, 1581–1592, 2001.

[4] Sheen, D. M., D. L. McMakin, W. M. Lechelt, and J. W. Griffin, "Circularly polarized millimeter-wave imaging for personnel screening," in *Passive Millimeter-Wave Imaging Technology VIII*, Vol. 5789, 117–126, Orlando, Florida, United States, 2005.

[5] Sheen, D. M., D. L. McMakin, T. E. Hall, and R. H. Severtsen, "Active millimeter-wave standoff and portal imaging techniques for personnel screening," in *2009 IEEE Conference on Technologies for Homeland Security*, 440–447, Waltham, MA, USA, 2009.

[6] Ahmed, S. S., A. Schiessl, and L.-P. Schmidt, "A novel fully electronic active real-time imager based on a planar multistatic sparse array," *IEEE Transactions on Microwave Theory and Techniques*, Vol. 59, No. 12, 3567–3576, 2011.

[7] Ahmed, S. S., A. Schiessl, and L.-P. Schmidt, "A novel active real-time digital-beamforming imager for personnel screening," in *9th European Conference on Synthetic Aperture Radar, EUSAR 2012*, 178–181, Nuremberg, Germany, 2012.

[8] Bertl, S. and J. Detlefsen, "Effects of a reflecting background on the results of active MMW SAR imaging of concealed objects," *IEEE Transactions on Geoscience and Remote Sensing*, Vol. 49, No. 10, 3745–3752, 2011.

[9] Liu, Y., "Research on millimetre wave passive detection target detection and identification algorithm," Ph.D. dissertation, University of Electronic Science and Technology, Chengdu, China, 2016.

[10] Tajdini, M. M., M. Asri, E. Wig, A. Gamage, and C. M. Rappaport, "Fast, fully-automatic characterization of metallic and water-based threat objects for millimeter-wave personnel screening systems," *IEEE Open Journal of Antennas and Propagation*, Vol. 4, 245–253, 2023.

[11] Yu, M., Y. Li, and J. Chen, "NUFFT-based algorithm for near-field MMW synthetic aperture imaging radiometers," in *Proceedings 2013 International Conference on Mechatronic Sciences, Electric Engineering and Computer (MEC)*, 527–531, Shenyang, China, 2014.

[12] Qiao, L., Y. Wang, Z. Shen, Z. Zhao, and Z. Chen, "Compressive sensing for direct millimeter-wave holographic imaging," *Applied Optics*, Vol. 54, No. 11, 3280–3289, 2015.

[13] Du, K., W. Wang, F. Nian, *et al.*, "Research on detection of hazardous materials carried by human body with active millimetre wave images," *System Engineering and Electronic Technology*, Vol. 38, No. 6, 1462–1468, 2016.

[14] Li, L. and S. Qin, "Real-time detection of hiding contraband in human body during the security check based on lightweight U-Net with deep learning," *Journal of Electronics & Information Technology*, Vol. 44, No. 10, 3435–3446, 2022.

[15] Yin, C., "Research on the simulation method of millimetre wave passive radiation imaging," Ph.D. dissertation, Nanjing University of Posts and Telecommunications, Nanjing, China, 2016.

[16] Li, X., "Simulation and experimental study of passive millimetre wave imaging on rough surfaces," Ph.D. dissertation, Huazhong University of Science and Technology, Wuhan, China, 2019.

[17] Li, X., A. Taflove, and V. Backman, "Modified FDTD near-to-far-field transformation for improved backscattering calculation of strongly forward-scattering objects," *IEEE Antennas and Wireless Propagation Letters*, Vol. 4, 35–38, 2005.

[18] Hanninen, I., M. Pitkonen, K. I. Nikoskinen, and J. Sarvas, "Method of moments analysis of the backscattering properties of a corrugated trihedral corner reflector," *IEEE Transactions on Antennas and Propagation*, Vol. 54, No. 4, 1167–1173, 2006.

[19] Collaro, A., G. Franceschetti, M. Migliaccio, and D. Riccio, "Gaussian rough surfaces and Kirchhoff approximation," *IEEE Transactions on Antennas and Propagation*, Vol. 47, No. 2, 392–398, 1999.

[20] Toporkov, J. V. and G. S. Brown, "Numerical study of the extended Kirchhoff approach and the lowest order small slope approximation for scattering from ocean-like surfaces: Doppler analysis," *IEEE Transactions on Antennas and Propagation*, Vol. 50, No. 4, 417–425, 2002.

[21] Hwang, H., J. Yim, J.-W. Cho, C. Cheon, and Y. Kwon, "110 GHz broadband measurement of permittivity on human epidermis using 1 mm coaxial probe," in *IEEE MTT-S International Microwave Symposium Digest, 2003*, Vol. 1, 399–402, Philadelphia, PA, USA, 2003.

[22] Sankaralingam, S. and B. Gupta, "Determination of dielectric constant of fabric materials and their use as substrates for design and development of antennas for wearable applications," *IEEE Transactions on Instrumentation and Measurement*, Vol. 59, No. 12, 3122–3130, 2010.

[23] Lamb, J. W., "Miscellaneous data on materials for millimetre and submillimetre optics," *International Journal of Infrared and Millimeter Waves*, Vol. 17, 1997–2034, 1996.

[24] Arik, E., H. Altan, and O. Esenturk, "Dielectric properties of diesel and gasoline by terahertz spectroscopy," *Journal of Infrared, Millimeter, and Terahertz Waves*, Vol. 35, 759–769, 2014.